

LETTER TO THE EDITOR

# The build-up of the cD halo of M87 - evidence for accretion in the last Gyr <sup>★</sup>

A. Longobardi<sup>1</sup>, M. Arnaboldi<sup>2</sup>, O. Gerhard<sup>1</sup>, J.C. Mihos<sup>3</sup>

<sup>1</sup> Max-Planck-Institut für Extraterrestrische Physik, Giessenbachstrasse, D-85741 Garching, Germany  
e-mail: alongobardi@mpe.mpg.de, gerhard@mpe.mpg.de

<sup>2</sup> European Southern Observatory, Karl-Schwarzschild-Strasse 2, D-85748 Garching, Germany  
e-mail: marnabol@eso.org

<sup>3</sup> Department of Physics and Astronomy, Case Western University, 10900 Euclid Avenue, Cleveland, OH 44106, USA  
e-mail: mihos@case.edu

in press, A&A

## ABSTRACT

**Aims.** We present kinematic and photometric evidence for an accretion event in the halo of the cD galaxy M87 in the last Gyr.

**Methods.** Using velocities for  $\sim 300$  planetary nebulas (PNs) in the M87 halo, we identify a chevron-like substructure in the PN phase-space. We implement a probabilistic Gaussian mixture model to identify PNs that belong to the chevron. From analysis of deep V-band images of M87, we find that the region with the highest density of chevron PNs is a crown-shaped substructure in the light.

**Results.** We assign a total of  $N_{\text{PN,sub}} = 54$  to the substructure, which extends over  $\sim 50$  kpc along the major axis where we also observe radial variations of the ellipticity profile and a colour gradient. The substructure has highest surface brightness in a  $20\text{kpc} \times 60\text{kpc}$  region around 70 kpc in radius. In this region, it causes an increase in surface brightness by  $\geq 60\%$ . The accretion event is consistent with a progenitor galaxy with a V-band luminosity of  $L = 2.8 \pm 1.0 \times 10^9 L_{\odot,V}$ , a colour of  $(B - V) = 0.76 \pm 0.05$ , and a stellar mass of  $M = 6.4 \pm 2.3 \times 10^9 M_{\odot}$ .

**Conclusions.** The accretion of this progenitor galaxy has caused an important modification of the outer halo of M87 in the last Gyr. By itself it is strong evidence that the galaxy's cD halo is growing through the accretion of smaller galaxies as predicted by hierarchical galaxy evolution models.

**Key words.** galaxies: clusters: individual (Virgo cluster) - galaxies: halos - galaxies: individual (M87) - planetary nebulas: general

## 1. Introduction

According to the current theory of hierarchical formation and evolution of structures, accretion events are believed to have an important role in the cosmological build up of stellar halos in elliptical galaxies (De Lucia & Blaizot 2007), responsible for their growth at relatively low redshifts ( $z < 2$ ; Oser et al. 2010). In dense environments accretion is even more dramatic, such that close to the dynamical centre of the cluster, central cluster galaxies are expected to have the majority of their stars accreted (Laporte et al. 2013; Cooper et al. 2014).

On the observational front, the outer stellar envelopes are observed to increase in mass by a factor of  $\sim 4$  since  $z = 2$  (van Dokkum et al. 2010). The presence of an accreted component is usually identified as an excess of light over the extrapolation of the galaxy's inner profile (Zibetti et al. 2005; Gonzalez et al. 2007; D'Souza et al. 2014), or by high Sersic indexes ( $n > 4$ ; Kormendy et al. 2009). Observations of blue colour gradients from the centres of early-type galaxies towards their outskirts (Peletier et al. 1990; Liu et al. 2005; Rudick et al. 2010), mainly attributed to a gradient in metallicity (Tamura et al. 2000; Loubser & Sánchez-Blázquez 2012; Montes et al. 2014) are also in agreement with a change in stellar properties driven

by the accretion of smaller systems. Records of accretion events are also revealed in the form of spatially extended low-surface brightness features in the outskirts of stellar halos (Mihos et al. 2005; van Dokkum et al. 2014; Duc et al. 2015). These *substructures* are not in a phase-mixed equilibrium in the host galaxy potential and, therefore, can in principle be traced as kinematic features in velocity phase-space.

M87 is one of the nearest central galaxies (at an adopted distance of 14.5 Mpc; Ciardullo et al. 2002; Longobardi et al. 2015), close to the dynamical centre of the Virgo cluster (Binggeli et al. 1987). It is considered a type-cD galaxy (Weil et al. 1997; Kormendy et al. 2009) with an extended stellar envelope that reaches  $\sim 150$  kpc in radius. A blue colour gradient towards its outskirts (Rudick et al. 2010) has been interpreted as age and metallicity gradients (Liu et al. 2005; Montes et al. 2014), consistent with a late build-up of its halo. The orbital properties of globular clusters (GCs) (Agnello et al. 2014) and ultra compact dwarfs (Zhang et al. 2015) also favour accretion onto the halo. M87 has been the target of several deep imaging surveys (Mihos et al. 2005; Rudick et al. 2010), and its close proximity has made it possible to identify hundreds of planetary nebulas (PNs), and to measure their line-of-sight velocities (LOSVs; Doherty et al. 2009; Longobardi et al. 2015).

In this letter we use the synergy between PN kinematics and deep imaging to identify an on-going accretion event in the outer halo of M87, which we find to be a non-negligible perturbation of the galaxy properties at the distances where it is traced.

Send offprint requests to: A. Longobardi

<sup>★</sup> Based on observations made with the VLT at Paranal Observatory under programs 088.B-0288(A) and 093.B-066(A), and with the SUBARU Telescope under program S10A-039.

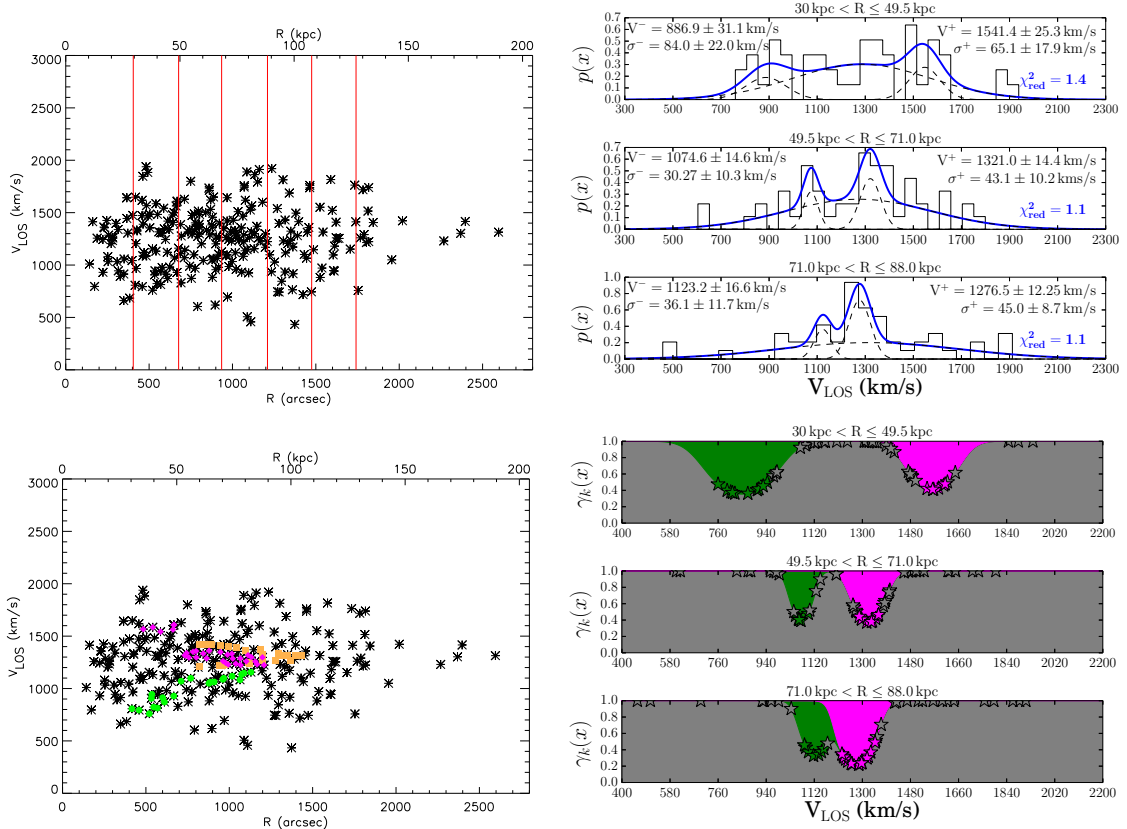


**Fig. 1.** **Top-left:** Projected phase-space,  $V_{\text{LOS}}$  vs. major axis distance ( $R$ ), for all spectroscopically confirmed PNs (black asterisks) in the halo of M87. Red lines separate the elliptical annuli analysed to isolate cold components associated to the substructure. **Top-right:** Histograms of the LOSVD in the three elliptical annuli. In each panel, the blue lines show the best-fit model computed as a combination of three Gaussians. Black-dashed lines show the relative contribution of each component to the LOSVD, with parameters for the cold components given in the plot. **Bottom-left:** As in the top-left panel, however, the green circles and magenta diamonds show the PNs associated with the cold secondary peaks in the LOSVD. Orange squares show a kinematically selected GC substructure from Romanowsky et al. (2012). **Bottom-right:** Probability that a PN is drawn from the halo component (dark grey area) or from the chevron (green, magenta areas). Stars represent PN probabilities at their measured  $V_{\text{LOS}}$ .

## 2. Kinematic evidence for an accretion event in M87

We acquired kinematic data from the FLAMES/VLT spectroscopic survey for a large sample of PNs in the outer regions of M87 (Longobardi et al. 2013, 2015). The total sample consists of 254 objects classified as M87 halo PNs and 44 intracluster PNs, for which we have obtained LOSVs with an estimated median velocity accuracy of  $4.2 \text{ km s}^{-1}$ . We concentrate here on the M87 halo PNs that cover a range of radii from  $\sim 15 - 150 \text{ kpc}$ .

We see a notable chevron (or “V” shape) structure in the projected phase-space of the PN sample as shown in Fig. 1 (top left). To isolate this kinematical substructure we utilise a three-component Gaussian mixture model to identify high-density, narrow features on top of a broader distribution. We note that there is not enough data to statistically favour this model over simpler models with BIC or AIC (Bayesian/Akaike Information Criteria; Liddle 2007); however, it is visually indicated and we will confirm it with photometry in Sec.4. A brief description of the technique is given in the following paragraph; for more details we refer the reader to Pedregosa et al. (2011).

A Gaussian Mixture Model (GMM) is a probabilistic model, which assumes that a distribution of points can be described as a

linear combination of  $K$  independent Gaussian probability density functions (PDFs), or components, expressed by:

$$p(x) = \sum_{k=1}^K p_k(x | \mu_k, \sigma_k) P_k, \quad (1)$$

where,  $x$  is a data vector (here the LOSVs),  $P_k$  is the mixture weight that satisfies the conditions  $0 \leq P_k \leq 1$  and  $\sum_{k=1}^K P_k = 1$ , and  $p(x | \mu_k, \sigma_k)$  are the individual Gaussian PDFs, with mean  $\mu_k$ , and dispersion  $\sigma_k$ . The GMM classifier implements the Expectation-Maximization (EM) algorithm, i.e. an iterative process that continuously updates the PDF parameters until convergence is reached. At the end of the EM procedure, the posterior probabilities,  $\gamma_k(x)$  for a data value to belong to each of the  $k$  Gaussian components are returned. These are described by:

$$\gamma_k(x) = \frac{p_k(x | \mu_k, \sigma_k) P_k}{p(x)}. \quad (2)$$

To apply the GMM to our LOSV distribution (LOVSD) we bin the PN M87 halo sample into seven elliptical annuli, or stripes in phase-space, covering the entire PN velocity phase-space. The LOSVD in each annulus is analysed as a combination of three Gaussians, where the centres ( $\mu_k$ ), widths ( $\sigma_k$ ), and weights ( $P_k$ ) are treated as free parameters in the EM algorithm, and have uncertainties  $\sigma_{\mu_k} = \sigma_k / \sqrt{S}$ ,  $\sigma_{\sigma_k} = \sigma_k / \sqrt{2S}$ , and  $\sigma_{P_k} = P_k / \sqrt{S}$ , with  $S = [\sum_n \gamma_k(x_n)]$  (MacKay 2003).

We find cold components in three out of seven elliptical bins, for which we show the histogram of the data, along with the best-fit GMM and reduced  $\chi^2$  in Fig. 1 (top-right panel). We also plot (bottom-left panel) the LOSV phase-space for the 254 PNs in the halo of M87: black crosses represent PNs of the smooth halo LOSVD of M87, while magenta diamonds and green dots are PNs that have a higher probability (see eq. 2) to belong to the chevron. Finally, we show the probability that a given PN is drawn from each of the components as a function of its velocity (bottom-right panel). The GMM assigned a total of 54 PNs to the chevron substructure, which covers  $700''$  ( $\sim 50$  kpc) for major axis distances  $500'' < R < 1200''$ . The separation,  $\Delta V$ , between the two peaks of the cold components becomes smaller at larger distances. For the three elliptical bins, it is  $\Delta V = 654.5 \pm 40.1$ ,  $246.4 \pm 20.5$ , and  $153.3 \pm 20.6$   $\text{kms}^{-1}$ , respectively. At  $R \sim 1200''$  ( $\sim 90$  kpc) the width of the chevron goes to zero with LOSVs close to the galaxy's systemic velocity ( $V_{\text{sys}} = 1275$   $\text{kms}^{-1}$ ; Longobardi et al. 2015)<sup>1</sup>. PNs on the arms of the chevron are seen on both the northern and southern sides of the galaxy as is shown in Fig. 2 (see Sect. 3). The broad Gaussian with average mean velocity  $\sim 1290$   $\text{kms}^{-1}$  and dispersion  $\sim 320$   $\text{kms}^{-1}$  in the three bins traces the M87 halo.

The search for kinematic features in the phase-space of GCs has resulted in the discovery of a similar chevron-like structure (Romanowsky et al. 2012), shown in Fig.1 above as orange squares. Though the morphology in the phase-space is similar it differs in a number of physical properties: the width goes to zero at  $R_{\text{GC}} \sim 1500''$  with  $V_{\text{LOS,GC}} = 1307$   $\text{kms}^{-1}$ , versus  $R \sim 1200''$  and  $V_{\text{LOS}} \sim 1250 \pm 21$   $\text{kms}^{-1}$  for the PNs. Moreover, the 27 chevron GCs show a very different spatial distribution with the highest density of points on the NE photometric minor axis (Romanowsky et al. 2012; D'Abrusco et al. 2015), and few GCs near the crown substructure traced by the PNs.

### 3. Localising the substructure with deep imaging

In Fig. 2 (left), we show the position of the chevron PNs overplotted on  $1.6 \times 1.6$   $\text{deg}^2$  V-band image of M87, with an estimated surface brightness limit of  $\mu_V = 28.5$   $\text{mag arcsec}^{-2}$  (Mihos et al. 2015). Here we see the large spatial extent of the substructure associated with the chevron PNs. Because of its shape on the image we will refer to it as the *veil of M87*. Now we are interested to see if this feature is also visible in the optical light.

To this end, we constructed an unsharped masked image, which is the difference between the original image and a smoothed image. We utilised the IRAF task `fmedian` to smooth the original image by using a window with a size of  $1450'' \times 1450''$ . This window size was chosen so that it contained the large scale extension of the substructure. By looking at the highest concentration of PNs, in the NW region of M87, it can be seen to extend over many hundreds of arcseconds ( $\sim 800''$ ). Thus, the adopted box size is  $\sim 1.8$  times larger than the long side of the feature.

The results of the unsharped masking can be seen in Fig. 2 (central panel), where the high frequency structures are now clearly visible. A previously unknown debris structure, with a crown-like shape, can be seen on top of M87 at the NW side. This we refer to as the *crown of M87's veil*. It has a characteristic width of  $\sim 300''$ , an extension of  $\sim 800''$ , and is almost perpendicular to M87's photometric major axis. Just as the PN

spatial distribution showed, the edge of this feature is found at  $R \sim 1200''$  ( $\sim 90$  kpc).

Over the same major axis distances at which the substructure is located, we also observe variations in the M87 ellipticity profile. Between  $300'' < R < 800''$  the ellipticity increases and then flattens to a value of  $e \sim 0.43$  for  $R > 800''$  (Kormendy et al. 2009). In particular, the region at which the gradient flattens reflects the crown-like overdensity.

## 4. Physical properties of the accreted satellite

### 4.1. Luminosity and $\alpha$ -parameter

To understand the physical origin of this structure, we compute its total luminosity. We do it in a region with size  $\sim 800'' \times 300''$ , after the subtraction of the local background, determined using a region photometry method (for more details see Rudick et al. 2010). We find a total luminosity in the range of  $L_{\text{crown}} = 3.7 \pm 0.9 \times 10^8 L_{\odot, V}$ . When compared to the luminosity determined in the same region from the original image,  $L \sim 5.9 \times 10^8 L_{\odot, V}$ , it is clear that at these distances the substructure represents a significant fraction,  $\sim 60\%$ , of the total light.

In the region of the crown we count  $N_{\text{PN, crown}} = 12 \pm 3$  PNs, while we find a total of  $N_{\text{PN, chevron}} = 54 \pm 7$  PNs associated to the entire chevron (see Sect. 2). By correcting these numbers for incompleteness factors as in Longobardi et al. (2015) these become 19 and 142, respectively. Hence, by scaling  $L_{\text{crown}}$  to the total number of PNs associated to the chevron we obtain the total luminosity associated to the progenitor of the M87 veil to be  $L \sim 2.8 \pm 1.0 \times 10^9 L_{\odot, V}$ .

The total number of PNs is proportional to the total bolometric luminosity of the parent stellar population, and the proportionality is quantified with the luminosity-specific PN density, or,  $\alpha$ -parameter (Buzzoni et al. 2006). Utilising the computed luminosity, and the completeness-corrected estimate for  $N_{\text{PN, chevron}}$ , we can calculate the  $\alpha$ -parameter for the progenitor of the substructure. Considering that the typical probability of the  $N_{\text{PN, chevron}}$  PN to belong to the chevron is  $\sim 0.7$  (Fig. 1), we obtain  $\alpha_{2.5} = 1.8 \pm 0.7 \times 10^{-8} N_{\text{PN}} L_{\odot, \text{bol}}^{-1}$ . Here  $\alpha_{2.5}$  is 2.5 mag down the luminosity function as in Longobardi et al. (2015), and we have assumed a bolometric correction for the V-band of  $BC_V = 0.85$  (Buzzoni et al. 2006) and  $BC_{\odot} = -0.07$  for the Sun.

### 4.2. Colour and Mass

In Fig. 2 (right panel) we show the chevron PNs overplotted on the B-V colour image of M87, that combines the V-band data (see Sect. 3) with deep B-band photometry with a surface brightness limit of  $\mu_B = 29$   $\text{mag arcsec}^{-2}$ . It is interesting to notice that close to  $R \sim 1200''$  the colour shows an azimuthal variance, such that along the photometric minor axis the measured values are redder (Mihos et al. 2015). This feature correlates with the spatial number density of the chevron PNs, showing a deficit in number along the photometric minor axis. This suggests that the bluer regions are the result of the accreted material on top the light from M87's halo. In particular, the crown structure is measured to have integrated colour  $(B - V) = 0.76 \pm 0.05$ .

(B-V) colour is a good estimator of the mass-to-light-ratio,  $\Upsilon^*$ , of the underlying stellar population. By adopting  $\Upsilon_V^* = 2.3$  for  $(B-V) = 0.76$  (McGaugh & Schombert 2014), the total stellar mass associated to the disrupted galaxy is then  $M = 6.4 \pm 2.3 \times 10^9 M_{\odot}$ .

From the distribution and velocities of chevron PNs in Fig. 2 a possible interpretation of the satellite orbit could be that it was

<sup>1</sup> The stability of the fitted parameters and the measured distance of the chevron edge were tested with 100 GMM runs for different mock data sets and initialisation values.



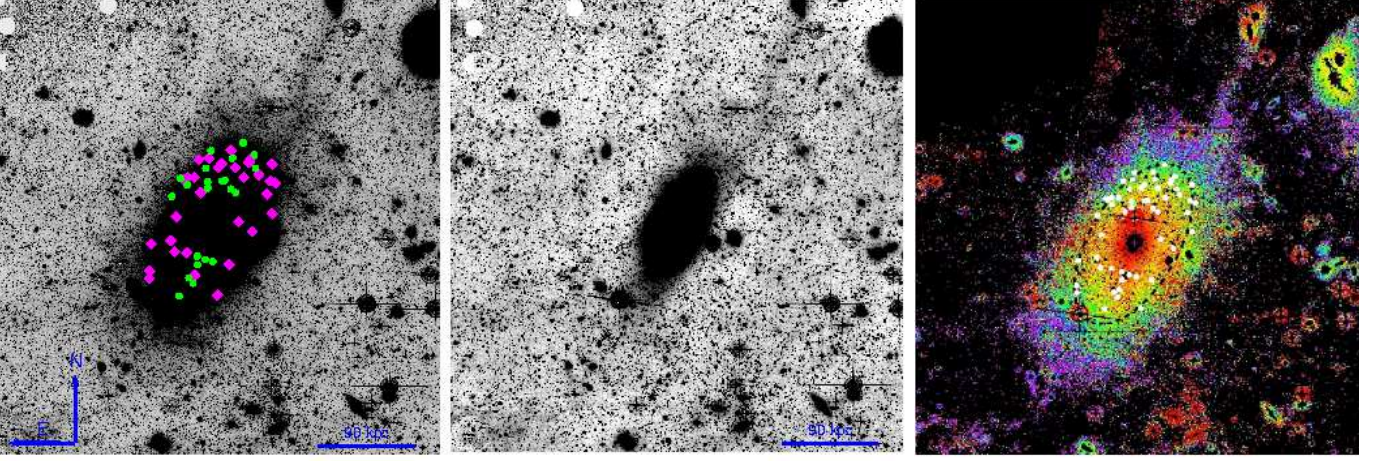


**Fig. 2.** Spatial and colour distribution associated with the kinematic substructure identified in the phase-space of the M87 halo PNs. **Left panel:** V-band image of a  $1.6 \times 1.6 \text{ deg}^2$  centred on M87 from Mihos et al. (2015). Full circles, and diamonds indicate the spatial position of the M87 halo PNs in the chevron substructure. Magenta and green colours indicate PN LOSVs above and below  $V_{\text{LOS}} = 1254 \text{ kms}^{-1}$ , the LOSV at the end of the chevron. **Central panel:** Unsharp masked image of M87 median binned to enhance faint structures. The crown-shaped substructure is visible at distance of  $800''\text{--}1200''$  ( $\sim 60\text{--}90 \text{ kpc}$ ) along the major axis, NW of M87. Details are given in Section 3. The blue line measures  $90 \text{ kpc}$ . **Right panel:** (B-V) colour image of M87 from Mihos et al. (2015) with chevron PNs overplotted (white dots). The dashed ellipse indicates the isophote at a major axis distance of  $1200''$ . The crown is found in a region where the (B-V) colour is on average 0.8, bluer than on the minor axis.

first disrupted entering M87 from the South (along the green dots), with the debris then moving up North, turning around in the crown region, and coming back down on both sides across M87 (the veil, magenta dots). The velocities would then imply that the northern side of M87 is closer to the observer. The dynamical time for such an orbit is of order  $\lesssim 1 \text{ Gyr}$  (Weil et al. 1997).

## 5. Summary and Conclusion

In this letter we have presented kinematic and photometric evidence for an accretion event in the halo of the cD galaxy M87. This event is traced by PNs whose velocity phase-space shows a distinct chevron-like feature, which is a result of the incomplete phase-space mixing of a disrupted galaxy. At major axis distances of  $R \sim 60\text{--}90 \text{ kpc}$ , where the width of the chevron goes to zero, a deep optical image shows the presence of a crown-like substructure that contributes  $\geq 60\%$  of the total light in this area.

The *crown* of M87’s *veil* is the densest part of the entire substructure, which covers  $\sim 50 \text{ kpc}$  along the major axis. In this region also a radial variation in M87’s ellipticity profile is observed. Looking at the spatial distribution of all the chevron PNs, it traces the azimuthal variation observed in the colour of M87, showing a deficit in number of tracers along the photometric minor axis where the galaxy is redder, and a higher fraction where the substructure is strongest and the colour is bluer.

We determined several physical properties of the disrupted satellite: a total luminosity of  $L = 2.8 \pm 1.0 \times 10^9 L_{\odot, V}$ , colour  $(B-V) = 0.76 \pm 0.05$ , and total stellar mass of  $M = 6.4 \pm 2.3 \times 10^9 M_{\odot}$ . The inferred value for the  $\alpha$ -parameter is  $\alpha = 1.8 \pm 0.7 \times 10^{-8} N_{\text{PN}} L_{\odot, \text{bol}}^{-1}$ . The similar colours of the accreted satellite and ICL suggest that the cD halo of M87 is presently growing by the accretion of similar star-forming systems as those that originate the diffuse IC component.

The evidence for on-going accretion in the outer halo of M87 is consistent with the observed size growth of giant elliptical galaxies and with predictions by theory. The presence of the

newly discovered substructure within the halo of M87 demonstrates, that beyond a distance of  $\sim 60 \text{ kpc}$ , its halo is still assembling.

*Acknowledgements.* AL is grateful to J. Elliott for helpful comments which improved the manuscript. JCM is supported by NSF grant 1108964.

## References

- Agnello, A., Evans, N. W., Romanowsky, A. J., & Brodie, J. P. 2014, MNRAS, 442, 3299
- Binggeli, B., Tammann, G. A., & Sandage, A. 1987, AJ, 94, 251
- Buzzoni, A., Arnaboldi, M., & Corradi, R. L. M. 2006, MNRAS, 368, 877
- Ciardullo, R., Feldmeier, J. J., Jacoby, G. H., et al. 2002, ApJ, 577, 31
- Cooper, A. P., Gao, L., Guo, Q., et al. 2014, ArXiv e-prints
- D’Abrusco, R., Fabbiano, G., & Zezas, A. 2015, ArXiv e-prints
- De Lucia, G. & Blaizot, J. 2007, MNRAS, 375, 2
- Doherty, M., Arnaboldi, M., Das, P., et al. 2009, A&A, 502, 771
- D’Souza, R., Kauffman, G., Wang, J., & Vegetti, S. 2014, MNRAS, 443, 1433
- Duc, P.-A., Cuillandre, J.-C., Karabal, E., et al. 2015, MNRAS, 446, 120
- Gonzalez, A. H., Zaritsky, D., & Zabludoff, A. I. 2007, ApJ, 666, 147
- Kormendy, J., Fisher, D. B., Cornell, M. E., & Bender, R. 2009, ApJS, 182, 216
- Laporte, C. F. P., White, S. D. M., Naab, T., & Gao, L. 2013, MNRAS, 435, 901
- Liddle, A. R. 2007, MNRAS, 377, L74
- Liu, Y., Zhou, X., Ma, J., et al. 2005, AJ, 129, 2628
- Longobardi, A., Arnaboldi, M., Gerhard, O., et al. 2013, A&A, 558, A42
- Longobardi, A., Arnaboldi, M., Gerhard, O., & Hanuschik, R. 2015, ArXiv e-prints
- Loubser, S. I. & Sánchez-Blázquez, P. 2012, MNRAS, 425, 841
- MacKay, D. J. 2003, Information theory, inference, and learning algorithms, Vol. 7 (Citeseer)
- McGaugh, S. S. & Schombert, J. M. 2014, AJ, 148, 77
- Mihos, J. C., Harding, P., Feldmeier, J., & Morrison, H. 2005, ApJ, 631, L41
- Mihos et al. 2015, in prep.
- Montes, M., Trujillo, I., Prieto, M. A., & Acosta-Pulido, J. A. 2014, MNRAS, 439, 990
- Oser, L., Ostriker, J. P., Naab, T., Johansson, P. H., & Burkert, A. 2010, ApJ, 725, 2312
- Pedregosa, F., Varoquaux, G., Gramfort, A., et al. 2011, Journal of Machine Learning Research, 12, 2825
- Peletier, R. F., Davies, R. L., Illingworth, G. D., Davis, L. E., & Cawson, M. 1990, AJ, 100, 1091
- Romanowsky, A. J., Strader, J., Brodie, J. P., et al. 2012, ApJ, 748, 29
- Rudick, C. S., Mihos, J. C., Harding, P., et al. 2010, ApJ, 720, 569

- Tamura, N., Kobayashi, C., Arimoto, N., Kodama, T., & Ohta, K. 2000, *AJ*, 119, 2134
- van Dokkum, P. G., Abraham, R., & Merritt, A. 2014, *ApJ*, 782, L24
- van Dokkum, P. G., Whitaker, K. E., Brammer, G., et al. 2010, *ApJ*, 709, 1018
- Weil, M. L., Bland-Hawthorn, J., & Malin, D. F. 1997, *ApJ*, 490, 664
- Zhang, H.-X., Peng, E. W., Côté, P., et al. 2015, *ApJ*, 802, 30
- Zibetti, S., White, S. D. M., Schneider, D. P., & Brinkmann, J. 2005, *MNRAS*, 358, 949